Water splitting-biosynthetic system with CO2 reduction efficiencies exceeding photosynthesis

Water Splitting-Biosynthetic System with CO_2 Reduction Efficiencies Exceeding Photosynthesis

Chong Liu,[1,3†] Brendan C. Colón,[2,†] Marika Ziesack,[2] Pamela A. Silver[2,*] and Daniel G. Nocera[1,*]

[1] Department of Chemistry and Chemical Biology, Harvard University, Cambridge, MA USA 02138

[2] Department of Systems Biology, Harvard Medical School, Boston, MA, USA 02115

[3] Division of Chemistry and Biological Chemistry, School of Physical and Mathematical Sciences, Nanyang Technological University, Singapore, 637371

[†] Contributed equally for this work

Abstract: Artificial photosynthetic systems can store solar energy and chemically reduce CO_2. We developed a hybrid water splitting-biosynthetic system based on a biocompatible earth-abundant inorganic catalyst system to split water into H_2 and O_2 at low driving voltages. When grown in contact with these catalysts, *Ralstonia eutropha* consumed the produced H_2 to synthesize biomass and fuels or chemical products from low CO_2 concentration in the presence of O_2. This scalable system has a CO_2-reduction energy efficiency of ~50% when producing bacterial biomass and liquid fusel alcohols, scrubbing 180 grams of CO_2, equivalent of 230,000 liters of air per 1 kWh of electricity. Coupling this hybrid device to existing photovoltaic systems would yield a CO_2 reduction energy efficiency of ~10%, exceeding natural photosynthetic systems.

Sunlight and its renewable counterparts are abundant energy sources for a sustainable society (*1*,*2*). Photosynthetic organisms harness solar radiation to build energy-rich organic molecules from water and CO_2. Numerous energy conversion bottlenecks in natural systems limit the overall efficiency of photosynthesis (*3*). Most plants do not exceed 1% and microalgae grown in bioreactors do not exceed 3%; however, efficiencies of 4% for plants and 5-7% for microalgae in bubble bioreactors may be achieved in the rapid (short term) growth phase (*3*). Artificial photosynthetic solar-to-fuels cycles may occur at higher intrinsic efficiencies (*4*–*7*) but they typically terminate at hydrogen (*8*), with no process installed to complete the cycle by carbon-fixation. This limitation may be overcome by interfacing H_2-oxidizing autotrophic microorganisms to electrodes that generate hydrogen or reducing equivalents directly (*9*–*14*).

We recently developed a hybrid inorganic-biological system that uses the catalysts of the artificial leaf (*15*,*16*) in combination with the bacterium *Ralstonia eutropha* (*17*) to drive an artificial photosynthetic process for carbon fixation into biomass and liquid fuels (*18*). In this system, water is split to oxygen by a cobalt phosphate (CoP_i) catalyst and hydrogen is produced by a NiMoZn alloy at applied voltages of E_{appl} = 3.0 V. Because the maximum energy efficiency is limited by the E_{appl} relative to the thermodynamic potential for water splitting (= E_{appl} / 1.23 V), a reduction in E_{appl} leads to biomass and liquid fuel efficiencies that surpasses previous integrated bioelectrochemical systems and is commensurate with natural photosynthetic yields (*18*). However, reactive oxygen species (ROS) produced at the cathode were detrimental to cell growth. Because hydrogen peroxide (H_2O_2), as well as short-lived superoxide ($O_2^{\bullet -}$) and hydroxyl radical ($HO^{\bullet}$) species are thermodynamically favored against H_2 production at pH = 7, ROS production dominated at or below the potential to generate H_2. When E_{appl} reached a sufficient overpotential to drive water splitting, H_2 production to support cell growth outweighed the toxic effects of ROS. In addition, the leaching of Ni from the NiMoZn alloy into solution inhibited microbial growth.

To develop a biocompatible catalyst system that is not toxic to the bacterium and lowers the overpotential for water splitting, we utilized a ROS-resistant cobalt-phosphorus (Co-P) alloy

cathode (Fig. 1A, pathway 1). This alloy drives the hydrogen evolution reaction (HER), while the self-healing CoPi anode (*19*,*20*) drives the oxygen evolution reaction (OER). The electrode pair works in concert to maintain extraneous cobalt ions at low concentration and to deliver low E_{appl} that split water to generate H_2 for *R. eutropha*, which support CO_2-reduction into complex organic molecules at high efficiency. The Co-P alloy, which is known to promote HER under alkaline solutions (*21*), exhibits high HER activity in water at neutral pH with minimal ROS production. X-ray photoelectron spectroscopy of Co-P thin films supports the elemental nature of the alloy (Fig. S1) and energy-dispersive X-ray spectroscopy (Fig. S2) establishes a 6 wt% phosphorus composition, which we have found to exhibit optimal HER activity in water at neutral pH with a Faradaic efficiency of 99 ± 2% (Fig. S3). Moreover, the activity of this Co-P alloy surpasses the activity of the earth-abundant NiMoZn and stainless steel (SS) cathodes used in previous studies (*18*) (Fig. 1B). At constant voltage, a stable HER current is maintained for at least 16 d (Fig. 1C). Negligible H_2O_2 is produced during HER (Fig. 1D), in contrast to that of simple metallic cathodes of Pt and SS.

The Co-P HER and CoP_i OER catalysts work in synergy to form a biocompatible water splitting system that salvages Co^{2+} cations leached from the electrodes (Fig. 1A, pathway 2). In the cyclic voltammogram of Co^{2+} in the phosphate buffer (pH = 7) (Fig. 1E), a pre-wave to the catalytic water-splitting current corresponds to the oxidation of Co^{2+} to Co^{3+}, which drives deposition of the catalyst. The CoP_i catalyst is also known to exhibit a deposition rate that is linearly proportional to Co^{2+} concentration (*22*). The self-healing property of CoP_i is derived from this interplay of the potential at which OER occurs *vs.* the potential at which the catalyst deposits (*20*). In concert, the Co-P and CoP_i catalysts preserve extremely low concentrations of Co^{2+} in solution through activity derived from the self-healing process. Inductively coupled plasma mass spectrometry (ICP-MS) analysis of a Co-P | CoP_i catalysts system (E_{appl} = 2.2 V) (*23*) show that sub-μM levels of Co^{2+} in solution after 24 h. This concentration of Co^{2+} (0.32 ± 0.06 μM) is well below the concentration of Co^{2+} (half maximal inhibitory concentration, IC_{50} ~ 25 μM) that is toxic to *R. eutropha* (Fig. S4). When diffusion between the two electrodes is

impeded by a porous glass frit, Co^{2+} concentrations rise to ~50 μM. We note for the NiMoZn cathode, Ni^{2+} concentrations are not regulated by self-healing as NiP_i cannot form from P_i (*24*), and the deposition to NiO_x occurs at >1.5 V *vs*. NHE (Fig. 1E; see Fig. S5 for comparison with potentials of relevant redox).

Interfacing the biocompatible Co-P | CoP_i water splitting catalysts with *R. eutropha* results in a system capable of CO_2-fixation. The CoP_i catalyst was deposited on a high-surface-area carbon cloth as the electrode support (Figs. 1A and S6), resulting in high currents (Fig. S7) and a faradaic efficiency of 96 ± 4% (Fig. S8). CO_2 reduction proceeded under a constant voltage within a batch reactor (Fig. S9), which was half-filled with a solution containing only inorganic salts (mostly phosphate) and trace metal supplements (*23*).

The CoP_i | Co-P | *R. eutropha* hybrid system can store over half its input energy as products of CO_2-fixation at low E_{appl} (Fig. 2A, Table S1). Entries 1-3 and 5 show that η_{elec} increases with decreasing E_{appl} under 100% CO_2 until $E_{appl} < 2.0$ V. Below $E_{appl} = 2.0$ V (Entry 8), a higher salt concentration (108 mM phosphate buffer) is required to facilitate mass transport and attendant current (Fig. S10). However, high salt concentrations are undesirable for *R. eutropha* metabolism. Thus a concentration of 36 mM phosphate and $E_{appl} = 2.0$ V resulted in optimal η_{elec}; the highest η_{elec} achieved for biomass production was 54 ± 4% (Entry 5, n = 4) over a duration of 6 d. Our CO_2 reduction efficiency is comparable to the highest demonstrated by *R. eutropha* during H_2-fermentation (*25*). This biomass yield is equivalent to assimilating ~4.1 mol (180 g) of CO_2 captured at the cost of 1 kWh of electricity. The amount of captured CO_2 is 1/10 of that caught by amine-based carbon capture and storage (~2000 g at the cost of 1 kWh) (*26*), whose processed product cannot be used as fuel. Enlarging the batch reactor volume by 10-fold did not perturb the efficiency (Entries 4 and 6), indicating that the system is scalable and the reactor volume does not pose immediate limits. Interestingly, the η_{elec} under air (400 ppm CO_2) is 20 ± 3% (Entry 7, n = 3), which is only 2.7 times lower than the case of pure CO_2 although the partial pressure of CO_2 is reduced by 2,500 times. This indicates that CO_2 is not a limiting reagent (*vide*

infra). The ~20% of η_{elec} for biomass is equivalent to assimilating ~1.5 mol of CO_2 captured from about 85,200 liters of air at ambient condition with the cost of 1 kWh of electricity.

We also isolated a ROS-resistant variant of *R. eutropha*, evolved from one SS | CoP_i water-splitting reactor after 11 consecutive days of operation (E_{appl} = 2.3 V) with a H_2O_2 generation rate of ~ 0.6 μM/min. Genome sequencing found several mutations between the strain (BC4) and the wild-type (H16) (Table S2). In the presence of paraquat as a ROS-inducer (*27*), the IC_{50} of paraquat for BC4 is almost one order of magnitude higher than that of wild type (Fig. S11). There is no significant benefit of BC4 strain with regard to η_{elec}, further confirming the absence of ROS in our system (*vide supra*). Nonetheless, BC4 should find great utility for achieving high η_{elec} in systems where ROS is problematic.

Biomass accumulation scales linearly with the amount of charge passed under pure CO_2 (Fig. 2B) or ambient CO_2 levels (Fig. 2C). The linear growth is accounted for by a model that combines governing equations for H_2-generation from water splitting and biomass accumulation from carbon-fixation (*23*). The model predicts a linear correlation between biomass and charge passed after an induction period of low population density of bacteria and high H_2 concentration (Figs. 2D and S12), which is consistent with the data shown in Figs. 2B and 2C where the induction period is too short to be observed. Gas chromatography measurements revealed a H_2 concentration in the reactor headspace of 0.19 ± 0.04% (n = 3) for 100% CO_2 and 0.10 ± 0.05% (n = 3) in air, which corresponded to 1.5 ± 0.3 and 0.8 ± 0.4 μM in water. These concentrations of H_2 are well below the Michaelis constant of ~6 μM for membrane-bound hydrogenases in *R. eutropha* (*28*), suggesting that H_2 is facilely consumed by *R. eutropha*. Moreover, similar linear growth conditions for both pure and ambient CO_2 atmospheres provide evidence that H_2 oxidation rather than CO_2 reduction is rate-limiting for biosynthesis. Lastly, *R. eutropha* halted growth during "night" cycles and continued CO_2 reduction 12 h later upon resumption of the water-splitting reaction (Fig. 2E), confirming the intrinsic dependence of *R. eutropha* on H_2 generation. These data also reveal that the CoP_i | Co-P | *R. eutropha* hybrid system is compatible with the intermittent nature of a solar energy source. Direct CO_2 reduction from air highlights the

relatively high affinity of *R. eutropha* for CO_2 at low pressures and at high O_2 concentrations, in contrast to the reported results of synthetic catalysts (*29*), individual enzymes (*30*,*31*), and strictly anaerobic organisms such as acetogens and methanogens (*11–14*) (Table S3).

Metabolic engineering of *R. eutropha* enables the renewable production of an array of fuels and chemical products (*17*). When *R. eutropha* confronts nutrient constraints coupled with carbon excess, the biosynthesis of poly(3-hydroxybutyrate) (PHB) is triggered in the wild-type H16 strain as an internal carbon storage (*17*). As such, digestion is necessary for PHB collection (*23*). Under a constant rate of water splitting, PHB synthesis was not manifest until nitrogen became limiting (~2 d), indicated by the cessation of biomass accumulation (Fig. 3A) as well as the η_{elec} of every 24 h (Fig. 3B and S13). With a titer of ~700 mg/L, the 6-d average for PHB synthesis is η_{elec} = 36 ± 3% (Fig. 2A, Entry 9) with a 24-h maximum of η_{elec} = 42 ± 2% (n = 3) (Fig. 3B). In engineered strains (*32*,*33*), this PHB pathway can be modified to excrete the fusel alcohols isopropanol (C_3), isobutanol (C_4), and 3-methyl-1-butanol (C_5) with energy densities of 24, 28, and 31 MJ/L, respectively. The culture supernatant is then analyzed to quantify the secreted alcohols (*23*). The accumulation of these liquid fuels follows similar trends as observed for PHB synthesis. Figs. 3C and 3E show that biomass production plateaus while isopropanol titers grow to ~600 mg/L and $C_4 + C_5$ alcohol titers grow to ~220 mg/L. Engineered *R. eutropha* strain produced isopropanol with a 6-d average η_{elec} = 31 ± 4% (Fig. 2A, Entry 10) with a 24-h maximum of η_{elec} = 39 ± 2% (n = 4) (Fig. 3D); strain engineered to produce $C_4 + C_5$ alcohols averaged a 6-d η_{elec} = 16 ± 2% (Fig. 2A, Entry 11) with a 24-h maximum of η_{elec} = 27 ± 4 % (n = 3) (Fig. 3F). The achieved titers are higher than previous reported values, and η_{elec} have been increased by at least 20 to 50 fold (*10*,*18*). *R. eutropha* has demonstrated tolerance towards isopropanol (Fig. S14), allowing for enriched product concentrations under extended operation.

Our combined catalyst design mitigates biotoxicity at a systems level, allowing water-splitting catalysis to be interfaced with engineered organisms to realize high CO_2 reduction efficiencies that exceed natural photosynthetic systems. Owing to low E_{appl} of 1.8 – 2.0 V for water splitting, high η_{elec} are achieved that translate directly to high solar-to-chemical efficiencies

(η_{SCE}) when coupled to typical solar-to-electricity device ($\eta_{SCE} = \eta_{solar} \times \eta_{elec}$). For a photovoltaic device of η_{solar} = 18%, the Co-P | CoP_i | *R. eutropha* hybrid system can achieve a η_{SCE} = 9.7% for biomass, 7.6% for bio-plastic, and 7.1% for fusel alcohols. This approach allows for the development of artificial photosynthesis with efficiencies well beyond natural photosynthesis, thus providing a platform for the distributed solar production of chemicals.

References and Notes

1. N. S. Lewis, D. G. Nocera, Powering the planet: Chemical challenges in solar energy utilization, *Proc. Natl. Acad. Sci. U.S.A.* **103**, 15729–15735 (2006).
2. N. S. Lewis, D. G. Nocera, The solar opportunity, *The Bridge* **46**, 41 (2015).
3. R. E. Blankenship *et al.*, Comparing photosynthetic and photovoltaic efficiencies and recognizing the potential for improvement, *Science* **332**, 805–809 (2011).
4. S. Licht *et. al.*, Over 18% solar energy conversion to generation of hydrogen fuel: theory and experiment for efficient solar water splitting, *Int. J. Hydrogen Energy*, **26**, 653–659 (2001).
5. F. F. Abdi *et. al*., Efficient solar water splitting by enhanced charge separation in a bismuth vanadate-silicon tandem photoelectrode, *Nature Commun.* **4**, 2195 (2013).
6. C. R. Cox, J. Z. Lee, D. G. Nocera, T. Buonassisi, Ten-percent solar-to-fuel conversion with nonprecious materials, *Proc. Natl. Acad. Sci. U.S.A.* **111**, 14057–14061 (2014).
7. J. Luo *et. al*., Water photolysis at 12.3% efficiency via perovskite photovoltaics and earth-abundant catalysts, *Science* **345**, 1593–1596 (2014).
8. T. R. Cook *et. al.*, Solar energy supply and storage for the legacy and nonlegacy worlds, *Chem. Rev.* **110**, 6474–6502 (2010).
9. T. Zhang, More efficient together, *Science* **350**, 738–739 (2015).
10. H. Li *et al.*, Integrated electromicrobial conversion of CO_2 to higher alcohols, *Science* **335**, 1596 (2012).
11. K. P. Nevin, T. L. Woodard, A. E. Franks, Z. M. Summers, D. R. Lovley, Microbial electrosynthesis: feeding microbes electricity to convert carbon dioxide and water to multicarbon extracellular organic compounds, *mBio* **1**, e00103–10 (2010).

12. S. Cheng, D. Xing, D. F. Call, B. E. Logan, Direct biological conversion of electrical current into methane by electromethanogenesis, *Environ. Sci. Technol.* **43**, 3953–3958 (2009).

13. C. Liu *et al.*, Nanowire–bacteria hybrids for unassisted solar carbon dioxide fixation to value-added chemicals, *Nano Lett.* **15**, 3634–3639 (2015).

14. E. M. Nichols *et al.*, Hybrid bioinorganic approach to solar-to-chemical conversion, *Proc. Natl. Acad. Sci. U.S.A.* **112**, 11461–11466 (2015).

15. M. W. Kanan, D. G. Nocera, In situ formation of an oxygen-evolving catalyst in neutral water containing phosphate and Co^{2+}, *Science* **321**, 1072–1075 (2008).

16. S. Y. Reece *et al.*, Wireless solar water splitting using silicon-based semiconductors and earth-abundant catalysts, *Science* **334**, 645–648 (2011).

17. A. Pohlmann *et al.*, Genome sequence of the bioplastic-producing "Knallgas" bacterium *Ralstonia eutropha* H16, *Nature Biotech.* **24**, 1257–1262 (2006).

18. J. P. Torella *et al.*, Efficient solar-to-fuels production from a hybrid microbial–water-splitting catalyst system, *Proc. Natl. Acad. Sci. U.S.A.* **112**, 2337–2342 (2015).

19. D. A. Lutterman, Y. Surendranath, D. G. Nocera, A self-healing oxygen-evolving catalyst, *J. Am. Chem. Soc.* **131**, 3838–3839 (2009).

20. D. K. Bediako, A. M. Ullman, D. G. Nocera, Catalytic oxygen evolution by cobalt oxido thin films, *Top. Curr. Chem.* **371**, 173–214 (2015).

21. I. Paseka, J. Velicka, Hydrogen evolution and hydrogen sorption on amorphous smooth Me-P(x) (Me: Ni, Co and FeNi) electrodes, *Electrochim. Acta* **42**, 237–242 (1997).

22. Y. Surendranath, D. A. Lutterman, Y. Liu, D. G. Nocera, Nucleation, growth, and repair of a cobalt-based oxygen evolving catalyst, *J. Am. Chem. Soc.* **134**, 6326–6336 (2012).

23. See Supplementary Materials on *Science* Online

24. M. Dincă, Y. Surendranath, D. Nocera, Nickel-borate oxygen-evolving catalyst that functions under benign conditions, *Proc. Natl. Acad. Sci. U.S.A.* **107**, 10337–10341 (2010).

25. J. Yu, A. Dow, S. Pingali, The energy efficiency of carbon dioxide fixation by a hydrogen-oxidizing bacteria, *Int. J. Hydrogen Energy*, **38**, 8683–8690 (2013)

26. G. T. Rochelle, Amine scrubbing for CO_2 capture, *Science* **325**, 1652–1654 (2009).

27. J. R. Roede, G. W. Miller, Paraquat, in *Encyclopedia of Toxicology*, P. Wexler, Ed. (Academic Press, ed. 3, 1984), pp 756–758.

28. M. Ludwig, J. A. Cracknill, K. A. Vincent, F. A. Armstrong, O. Lenz, Oxygen-tolerant H_2 oxidation by membrane-bound [NiFe] hydrogenases of *Ralstonia* species, *J. Biol. Chem.* **284**, 465–477 (2009).

29. A. M. Appel *et. al*., Frontiers, opportunities, and challenges in biochemical and chemical catalysis of CO_2 fixation. *Chem. Rev.* **113**, 6621–6658 (2013).

30. A. Parkin, J. Seravalli, K. A. Vincent, S. W. Ragsdale, F. A. Armstrong, Rapid and efficient electrocatalytic CO_2/CO interconversions by *Carboxydothermus hydrogenoformans* CO dehydrogenase I on an electrode, *J. Am. Chem. Soc.* **129**, 10328–10329 (2007).

31. T. Reda, C. M. Plugge, N. J. Abram, J. Hirst, Reversible interconversion of carbon dioxide and formate by an electroactive enzyme, *Proc. Natl. Acad. Sci. U.S.A.* **105**, 10654–10658 (2008).

32. E. Grousseau, J. Lu, N. Gorret, S. Guillouet, A. Sinskey, Isopropanol production with engineered *Cupriavidus necator* as bioproduction platform, *Appl. Microbiol. Biotechnol.* **98**, 4277–4290 (2014).

33. J. Lu, C. Brigham, C. Gai, A. Sinskey, Studies on the production of branched-chain alcohols in engineered *Ralstonia eutropha*, *Appl. Microbiol. Biotechnol.* **96**, 283–297 (2012).

Acknowledgements: We thank N. Li for ICP-MS measurement, reagents; J. Torella, C. Myhrvold, C. Lemon, and M. Huynh for helpful discussions. C. L. acknowledges Prof. X. Ling at Nanyang Technological University, and financial support from Lee Kuan Yew Postdoctoral

Fellowship. B. C. acknowledges NSF Graduate Research Fellowships Program for a predoctoral fellowship. This work was supported by Office of Naval Research Multidisciplinary University Research Initiative Award N00014-11-1-0725 (P.A.S), Air Force Office of Scientific Research Grant FA9550-09-1-0689 (D.G.N.), and the Wyss Institute for Biologically Inspired Engineering (P.A.S.). We also acknowledge the TomKat Foundation and Harvard University Climate Change Solutions Fund for their support of this work. Harvard University and Harvard Medical School have filed a patent application on the technology described in this paper. The genome sequences are accessible in the NCBI SRA database under the accession number SRP073266.

SUPPLEMENTARY MATERIALS

Methods

Table S1 to S3

Figs. S1 to S14

Additional References (*34–49*)

Fig. 1. Active water-splitting catalyst pair with minimal biological toxicity. A, Reaction diagram and scanning electron microscopy images for Co-P alloy cathode and CoP_i anode. The main water-splitting reaction is colored in black, and the side reactions that yield toxicants are in red. Scale bars: 10 μm. **B**, *I-V* characteristics of different HER catalysts (pH 7, 10 mV/sec). **C**, 16-d chronoamperometry demonstrates the stability of Co-P cathode. **D**, Assay of H_2O_2 accumulation for various cathodes combining with CoP_i anode: yellow, Pt; blue, stainless steel (SS); red, Co-P alloy. E_{appl} = 2.2 V. n = 3. **E**, Cyclic voltammetry of Co^{2+} and Ni^{2+} in the presence of phosphate (P_i). Metal concentrations are both 0.5 mM, 50 mV/sec. The curve for Ni^{2+} is magnified by 50 times.

Fig. 2. Energy efficiencies η_{elec} and kinetics of the hybrid CO_2-reduction device. A, η_{elec} for the production of biomass and chemicals at different E_{appl} and various configurations (Table S1). The solid bars are averages of 5–6 d, while the dashed ones are 24-h maximum. n ≥ 3. **B** & **C**, The OD_{600}, indictor of biomass accumulation, and the amounts of electric charges that were passed, are plotted *vs.* the duration of experiments with 100% CO_2 (**B**) and air (**C**) in the headspace at 1 atm pressure. E_{appl} = 2.0 V. **D**, A microbial growth model predicts linear correlation between electric charges and biomass accumulation (Fig. S12). **E**, Real-time monitor of biomass accumulation under "day"/"night" cycle test.

Fig. 3. Efficient synthesis of selective chemicals from CO_2 and water. PHB (**A**, **B**), isopropanol (C_3) (**C**, **D**), C_4 and C_5 alcohols (**E**, **F**) were selectively produced from the hybrid device. **A**, **C**, and **E**, The OD_{600}, concentrations of selective chemicals, and charges passed through the electrodes are plotted *vs.* the duration of experiments. **B**, **D**, and **F**, The averaged η_{elec} for different products at every interval of 24 h. The overall η_{elec} combining biomass and chemical formation are listed as well. The η_{elec} of biomass, defined as intracellular organics exclude PHB, has been corrected to exclude the PHB interference in **B** (*23*) (see Fig. S13 for values before correction).

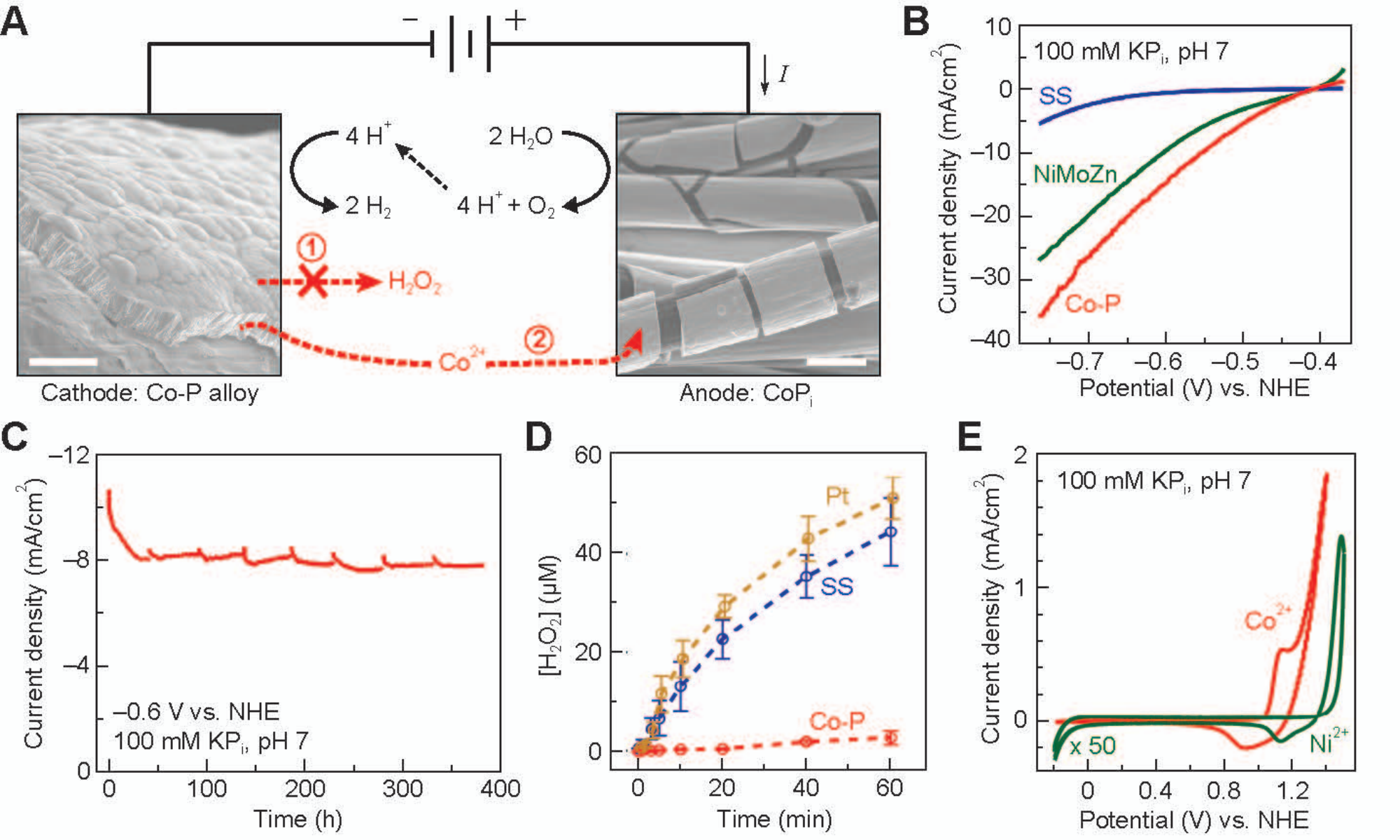
A
−
+
I
4 H+
2 H2O
2 H2
4 H+ + O2
①
H2O2
②
Co2+
Cathode: Co-P alloy
Anode: CoPi
B
100 mM KPi, pH 7
SS
NiMoZn
Co-P
Current density (mA/cm2)
Potential (V) vs. NHE
C
−0.6 V vs. NHE
100 mM KPi, pH 7
Current density (mA/cm2)
Time (h)
D
Pt
SS
Co-P
[H2O2] (μM)
Time (min)
E
100 mM KPi, pH 7
Co2+
Ni2+
x 50
Current density (mA/cm2)
Potential (V) vs. NHE

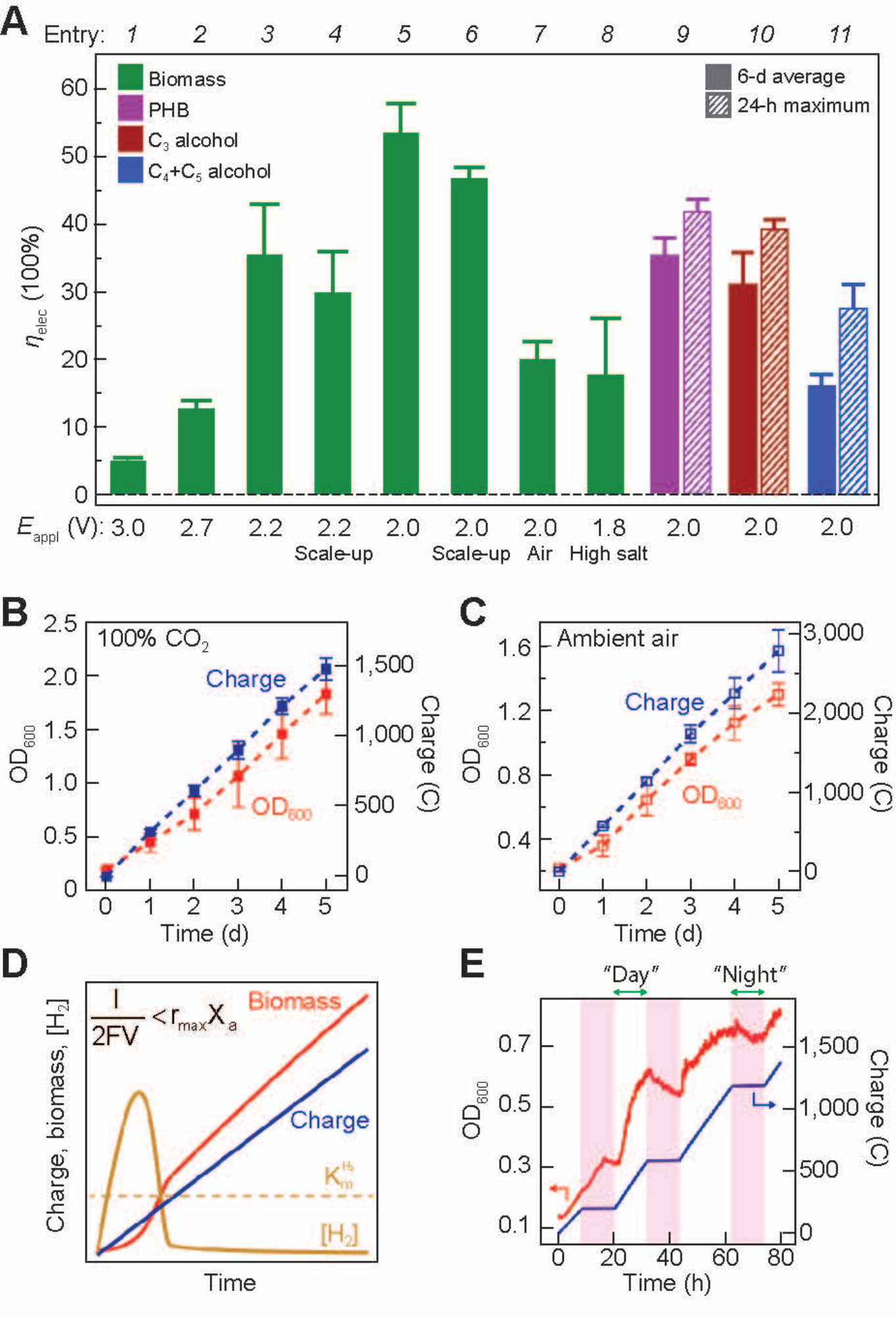
A
Entry: 1 2 3 4 5 6 7 8 9 10 11
Biomass
PHB
C3 alcohol
C4+C5 alcohol
6-d average
24-h maximum
ηelec (100%)
Eappl (V): 3.0 2.7 2.2 2.2 2.0 2.0 2.0 1.8 2.0 2.0 2.0
Scale-up
Scale-up
Air
High salt
B
100% CO2
Charge
OD600
Charge (C)
Time (d)
C
Ambient air
Charge
OD600
Charge (C)
Time (d)
D
I/2FV < rmax Xa
Biomass
Charge
Charge, biomass, [H2]
Time
E
"Day"
"Night"
OD600
Charge (C)
Time (h)

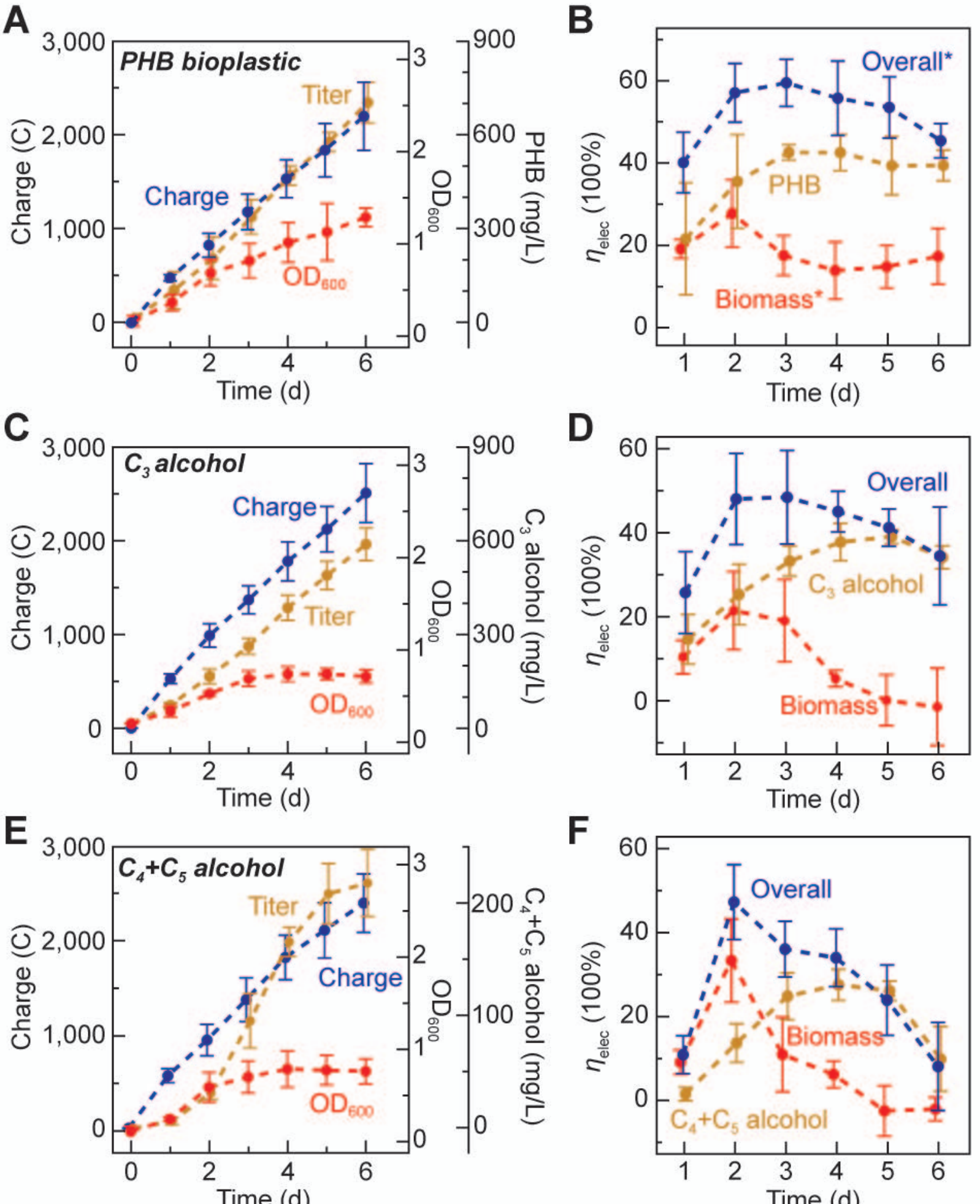
A
PHB bioplastic
Titer
Charge
OD600
Charge (C)
PHB (mg/L)
Time (d)
B
Overall*
PHB
Biomass*
ηelec (100%)
Time (d)
C
C3 alcohol
Charge
Titer
OD600
Charge (C)
C3 alcohol (mg/L)
Time (d)
D
Overall
C3 alcohol
Biomass
ηelec (100%)
Time (d)
E
C4+C5 alcohol
Titer
Charge
OD600
Charge (C)
C4+C5 alcohol (mg/L)
Time (d)
F
Overall
Biomass
C4+C5 alcohol
ηelec (100%)
Time (d)

Supporting Information

Water Splitting-Biosynthetic System with CO_2 Reduction Efficiencies Exceeding Photosynthesis

Chong Liu,[1,3†] Brendan C. Colón,[2,†] Marika Ziesack,[2] Pamela A. Silver[2,*] and Daniel G. Nocera[1,*]

[1] Department of Chemistry and Chemical Biology, Harvard University, Cambridge, MA USA 02138. [2] Department of Systems Biology, Harvard Medical School, Boston, MA, USA 02115. [3] Division of Chemistry and Biological Chemistry, School of Physical and Mathematical Sciences, Nanyang Technological University, Singapore, 637371.

[†] Contributed equally for this work

E-mail: Pamela_silver@hms.harvard.edu, dnocera@fas.harvard.edu.

Methods

Materials and chemicals. All materials and chemicals were used as received. Cobalt nitrate hexahydrate ($Co(NO_3)_2 \cdot 6H_2O$), boric acid (H_3BO_3), sodium chloride (NaCl), cobalt chloride hexachloride ($CoCl_2 \cdot 6H_2O$) were purchased from Sigma-Aldrich. Methyl-phosphonic acid and 316 stainless steel (SS) mesh were supplied from Alfa Aesar. Avcarb 1071 HCB carbon cloth (CC) was purchased from Fuel Cell Earth.

The catalysts for hydrogen evolution reaction (HER) and oxygen evolution reaction (OER) were created by electrochemical deposition methods with the use of a Gamry Interface 1000 potentiostat. A classic three-electrode setup was applied with Ag/AgCl, 1 M KCl reference electrode. After the deposition of catalysts, the electrodes were rinsed with ample deionized water.

The synthesis of CoP_i catalysts follows the procedures from previous reports (*15,34,35*). The deposition solution contains 10 mM $Co(NO_3)_2$ and 0.1 M methylphosphonate (MeP_i) buffer (pH 8). Two different conductive materials, 316 SS mesh and un-treated carbon cloth were applied as electrode substrates. The deposition was performed at 0.85 V *vs.* reference until the desired amount of charge was passed through. For the SS substrate, 50 mC/cm^2 of charge was passed before deposition stopped. Deposition onto carbon cloth stopped at 500 mC/cm^2.

Co-P alloy catalysts for HER are deposited via a cathodic electrodeposition strategy adopted from previous literature (*21*). The mechanism of its HER activity has previously been characterized in detail (*21*). The deposition solution contains 0.15 M H_3BO_3, 0.1 M NaCl, 0.33 M $Na_2H_2PO_2$, and 0.2 M $CoCl_2$. Clean SS mesh electrodes were biased at –1.2 V *vs.* reference for 15 min.

Electrode characterization. The morphologies of synthesized catalysts were imaged by Zeiss Supra 55VP field emission scanning electron microscope (FE-SEM) equipped with an energy-dispersive X-ray (EDX) spectroscopy. The chemical composition was also characterized by X-ray photoelectron spectrometry (XPS, Thermo Scientific K-Alpha). A Gamry Interface 1000 potentiostat was used for electrochemical characterization. A conventional three-electrode setup was employed for the analysis of individual electrodes; while a two-electrode setup similar as the one in bioelectrochemical reactor was used to benchmark the pair of water-splitting electrodes. The faradaic efficiencies of HER and OER were determined in a custom-built two-compartment electrochemical cell, whose gas outlet was connected to a gas chromatography (GC) equipped with a thermal conductivity detector (multiple gas analyzer #3, SRI Instrument).

Bioelectrochemical reactor. The water splitting and bacterial CO_2 fixation took place in a single enclosed chamber filled with CO_2 in the headspace (Fig. S9). The reported data are based on at least three biological replicates ($n \geq 3$). A Gamry Reference 600 potentiostat

coupled with an ECM8 electrochemical multiplexer allowed for parallel experiments of 8 reactors. The reactor consists of a 250 mL Duran® GL 45 glass bottle capped with a Duran® GL 45 3-ports (GL 14) connection system. The glass bottle was immersed in a 30 °C water bath. Two of the GL 14 screw cap ports served as the feedthroughs for the two water-splitting electrodes, and the third was used as the gas inlet regulated by a quarter-turn valve. For a typical experiment, 100 mL of all-inorganic minimal media solution was added into the reactor and water splitting was performed via a two-electrode system; the electrodes had a 4 cm^2 geometric area. The applied potential, E_{appl}, is defined as the voltage difference between the working and counter/reference electrodes in a two-electrode configuration; E_{appl} is detailed in Table S1 for each experiment. After inoculation with *R. eutropha* strains (initial OD_{600} = 0.2), the reactor was purged with CO_2 and then sealed. The experiments were stirred at 350 rpm by a triangular stirring rod to facilitate mass transport within the reactors. The bioelectrochemical reactor headspace was sampled daily using Supel™ inert foil gas sampling bags. The electrolyte was also sampled daily to quantify OD_{600} and product titers. After sampling, the reactor headspace was sparged to refill CO_2 in the headspace. In the case of CO_2 reduction directly from air, the reactor chamber was not isolated to the environment. The gas inlet port was connected to the ambient atmosphere through a 0.2 μm PVDF gas filter and no CO_2 gas flow was supplied to the reactor headspace. In this setup, the reactor headspace was in direct exchange with ambient environment through the PVDF filter.

The batch reactor design may be modified to a flow-based configuration, in which microbe-containing media would be forced to flow through the chamber where water splitting occurs. The low level of residual H_2 gas measured in the headspace indicates the efficient uptake of H_2 and accordingly a small energy loss would be expected under a flow reactor configuration.

Real-time monitoring of biomass accumulation was accomplished by measuring the optical density of the 100 mL reactor on a home-built setup with 20 sec time interval. A 650 nm laser pointer (Digi-Key Electronic) was directed at a photodiode across the 100 mL reactor containing bacteria and water splitting electrodes. Controlled through a customized script in MATLAB, every 20 sec the intensity of incident light after scattering the culture was determined with the help of an operational amplifier (Digi-Key Electronic.). A standard curve between the measured light intensity and OD_{600} was established, after measuring the transmitted light from *R. eutropha* cultures of known OD_{600} values. The OD_{600} decrease during the "dark" phase of the day/night cycle experiments is due to a loss of biomass (Fig. 2E). Without a source of energy during lithotrophic growth, cells lyse and OD_{600} drops. The growth in the first "night" phase may be due to the residual, unconsumed H_2 that remains from the previous "day" phase. With higher culture density, there was no excessive H_2 in the second and third "night" phases, and OD_{600} subsequently decreased. The differences in

biomass loss between the second and third "night" phases is likely due to the conditioning of H_2 scarcity as the population grows.

For a 10-fold scale-up experiment, a similar reactor was used but of 1000 mL volume. Unless noted, the procedure is similar as that employed for experiments using the 100 mL reactor. A Vacu-Quik jar system (Almore International, inc.) was modified with two current feedthroughs for water splitting electrodes and two PEEK tubes as gas inlet/outlet. A Neslab EX-211 constant temperature bath circulated water around the jar to maintain a temperature of 30 °C. For optimized temperature homogeneity, the jar and the water circulation was embedded in a thermally insulating layer. The volume of minimal medium solution was 1000 mL, and the size of electrodes was increased proportionally. The reactor was inoculated with *R. eutropha* (OD_{600} = 0.05) and grown under H_2/CO_2/air overnight. Before CO_2 reduction was begun, the initial OD_{600} of the experiment was recorded, typically between 0.15 and 0.20. The headspace of the reactor was thoroughly purged with CO_2 to remove the residual H_2 that remained from the autotrophic growth.

Facilitating CO_2 mass transport by pressurization is not beneficial in our current experiments, although such conditions may be helpful for larger reactors. Pressurization in the batch reactor risks acidifying the media and poses no advantages for the selectivity of ribulose-biphosphate carboxylase-oxygenase (RuBisCO) for CO_2 over O_2, which plateaus at ~10% CO_2 at 1 atm (*3*).

Bacterial strains and growth protocols. Unless noted, the composition of the minimal medium was 6.74 g/L $Na_2HPO_4{\cdot}7H_2O$, 1.5 g/L KH_2PO_4, 1.0 g/L $(NH_4)_2SO_4$, 80 mg/L $MgSO_4{\cdot}7H_2O$, 1 mg/L $CaSO_4{\cdot}2H_2O$, 0.56 mg/L $NiSO_4{\cdot}7H_2O$, 0.4 mg/L ferric citrate, and 200 mg/L $NaHCO_3$. Because nitrogen (N), phosphorous (P) and sulfur (S) are contributing about 10% (for N) and less than 5% (for P and S) of the total dry cell weight (*36*,*37*), the requirement of inorganic elements is not limiting the CO_2-reduction process under our experimental conditions. The constant renewal of "living" biocatalysts does not factor into the consumption of inorganic elements, because new bacteria can recycle the elements released from the expired microbes. This medium composition has a phosphate buffer concentration of 36 mM. For nitrogen-limited growth to produce isopropanol and PHB, the $(NH_4)_2SO_4$ concentration was reduced to 0.167 g/L. For experiments with higher salinity, the buffer strength of phosphate was increased by three times: 20.22 g/L $Na_2HPO_4{\cdot}7H_2O$, 4.5 g/L KH_2PO_4. This "high salt" medium has a phosphate buffer concentration of 108 mM. All solutions were filter-sterilized prior to use except the ferric citrate component, which was added after the filter sterilization step.

$NaHCO_3$ is added to the initial media preparation to maintain ionic strength and osmotic pressure. As a conjugate base under equilibrium with CO_2 in aqueous solution, bicarbonate can serve as carbon source for CO_2 reduction. *R. eutropha* converts bicarbonate to CO_2

through carbonic anhydrase. The prepared media has been fully equilibrated before any experiments take place.

R. eutropha H16 (wild type), Re2133-pEG12 and Re2410-pJL26 strains were obtained from Sinskey laboratory at MIT and the latter two has been described before (*32*,*33*). A ROS-resistant strain (BC4) was isolated that was evolved from 11 consecutive days of exposure to a SS | CoP_i water-splitting system (E_{appl} = 2.3 V). No growth was observed until day 7 when the OD_{600} rose from 0.15 to 1.15 over the next 4 days. Isolated strains were sequenced and mutations were compiled using *breseq* (*38*).

Growth protocols follow the procedures in literature (*18*). Unless noted, all of the microbial growth was at 30 °C. In general, individual colonies were picked from agar plates and inoculated into rich broth media solutions for overnight growth. Cultures were centrifuged and re-suspended in minimal medium supplemented with gentamicin (10 μg/mL). The cultures were placed in a Vacu-Quick jar filled with H_2 (8 mmHg) and CO_2 (2 mmHg) with air as balance. At this condition, *R. eutropha* adapted to autotrophic metabolism with H_2 as substrate.

Toxicant quantification. Abiotic water splitting was performed in the bioelectrochemical reactor using minimal medium solution as the electrolyte with a number of electrode combinations. 50 μL of electrolyte was transferred at a series of time points to a 96-well plate (Corning). The plate was kept on ice, in the dark, for no more than 1 hour prior to measurement. The H_2O_2 concentration was assayed using Amplex Red H_2O_2 detection kit (Sigma-Aldrich) by monitoring the absorbance at 555 nm using BIO-13 Synergy H1m plate reader. The concentration of H_2O_2 was quantified by comparing against a standard curve generated from H_2O_2 standards ranging from 0 to 40 μM.

The leaching rates of various elements from the electrodes were measured with inductively coupled plasma mass spectrometry (Thermo Electron, X-Series ICP-MS with collision cell technology, CCT). After running the abiotic water-splitting experiments for 24 hours at constant E_{appl}, 0.5 mL of electrolyte was sampled and diluted with 3.5 mL of 2% double distilled nitric acid (Sigma-Aldrich). Samples along with calibration standards were scanned twice for 60 sec each for ^{60}Ni, ^{59}Co, and ^{194}Pt. To demonstrate the "self-healing" effect of CoP_i anode on the metals leached from cathode, experiments were conducted in both one- and two-compartment electrochemical cells. In the single-compartment setup, both the HER cathode and OER anode were immersed in the same reactor. In the two-compartment setup (H-cell), a glass frit junction of fine porosity separated the two chambers and hindered the mass transport of leached metals.

The procedure for spot assays was performed by diluting 100 μL of culture grown under different conditions by 1:10 in fresh minimal medium, which was vortexed. Three to four serial 10-fold dilutions were made and 2 μL of each dilution was spotted on rich broth agar

plates and allowed to dry. Plates were typically grown for 2 days at 30 °C before imaging. The half maximal inhibitory concentration (IC_{50}) was estimated based on the comparison at 1/100 dilution. The areas of colonies at certain conditions were compared with that of control samples.

Quantification of titers. The amount of isopropanol and PHB produced were determined using a high performance liquid chromatography (HPLC, Agilent HPLC 1200) equipped with an Aminex HPX-87H column (*13,18*). The volume of each sample injection was 100 μL. The mobile phase was 2.5 mM H_2SO_4 aqueous solution, with a flow rate of 0.5 mL/min for either 30 min (isopropanol) or 60 min (PHB). 5 mM sodium acetate (Sigma-Aldrich) was added as an internal standard. Refractive index detector (isopropanol) and UV absorption detector (PHB) were used. The isopropanol assay measured the isopropanol concentration in the supernatant of thawed samples after centrifugation at 10000 rpm for 10 min. For PHB analysis, the centrifuged pellet was digested with concentrated H_2SO_4 at 90 °C for 60 min. The digestion solution was diluted with DI H_2O by 50 times and then passed through 0.2 μm filter. The concentrations of chemicals were determined by comparing the peak area with that in standard curves from 0.1 ~ 30 mM.

The titers of isobutanol and 3-methyl-1-butanol were characterized by a GC interfaced with quadropole Mass Spectrometer (Agilent 6890/5975 GC-MS) (*33*). A DB-WAX column (Agilent, 30 m × 0.32 mm × 0.5 μm) was applied, and 2 μL sample was injected with a split ratio of 20:1. Prior to GC-MS characterization, culture aliquots were centrifuged, and organic alcohols were extracted from the supernatant using chloroform at a 1:1 volume ratio.

Efficiency calculations. The efficiency values reported in this work are based on the statistical averages of at least three biological replicates. The calculations are conducted similarly as approaches in previous literatures (*13,18*). Here we define the electricity-to-organic efficiency as follows:

$$\eta_{elec} = \frac{\Delta_r G^o \text{ gain from } CO_2 \text{ to organic}}{\text{charge passed through (C)} \times \text{applied voltage (V)}}$$

"Organic" refers to the targeted product in the bioelectrochemical reactor, including biomass, isopropanol, PHB, C_4 and C_5 alcohols. The Gibbs free energy gains ($\Delta_r G^o$) for specific target products, along with the corresponding chemical reactions, are listed in the following:

Biomass formation:

$$CO_2(g) + 0.24\ NH_3(aq) + 0.525\ H_2O\ (\ell) \rightarrow CH_{1.77}O_{0.49}N_{0.24}(s) + 1.02\ O_2(g)$$
$$\Delta_r G^o = 479\ \text{kJ/mol}$$

PHB formation:

$4n\ CO_2(g) + 3n\ H_2O(\ell) \rightarrow (C_4H_6O_2)_n(s) + 4.5n\ O_2(g)$
$\Delta_rG^o \sim \Delta_rH^o = 1903$ kJ/mol per monomer

Isopropanol (C_3):

$3\ CO_2(g) + 4\ H_2O(\ell) \rightarrow C_3H_8O\ (\ell) + 4.5\ O_2(g)$
$\Delta_rG^o = 1951$ kJ/mol

Isobutanol (2-methyl-1-propanol, C_4):

$4\ CO_2(g) + 5\ H_2O(\ell) \rightarrow C_4H_{10}O\ (\ell) + 6\ O_2(g)$
$\Delta_rG^o = 2597$ kJ/mol

Isopentanol (3-methyl-1-butanol, C_5):

$5\ CO_2(g) + 6\ H_2O(\ell) \rightarrow C_5H_{12}O\ (\ell) + 7.5\ O_2(g)$
$\Delta_rG^o = 3326$ kJ/mol

The reported efficiencies were calculated based on the above thermodynamic values. The Δ_rG^o value for biomass is based on the report that the Gibbs free energy of formation of biomass in *Escherichia coli* is –46 kJ/mol carbon (*39*), and experimentally the efficiency was calculated based on the relationship: 1 OD_{600} = 0.448 g/L dry biomass (*40*). The Gibbs formation energy value of PHB was approximated by the enthalpy of its combustion, which was determined experimentally using oxygen bomb calorimeter (Parr 6725EA). Experimentally, it was observed that the accumulation of PHB increased OD_{600} values, which could lead to overestimated efficiency of biomass production (*41–43*). For the case where biomass is defined as the intracellular organics excluding PHB, light scattering from PHB can be accounted for. The OD_{600} increase between day 3 and day 6 in Fig. 3A is correlated to the accumulation of PHB rather than biomass, as OD_{600} plateaued for non-PHB producing strains (Figs. 3C and 3E). A linear fit of OD_{600} and PHB titers (C_{PHB}) between day 3 and day 6 shows that 831 mg/L PHB is equivalent to 1.0 OD_{600}. Given this, the effective OD_{600} caused by biomass only ($OD_{biomass}$) was calculated according to the following equation:

$$OD_{biomass} = OD_{600} - \frac{C_{PHB}\ (mg \cdot L^{-1})}{831\ mg \cdot L^{-1} \cdot OD^{-1}}$$

The apparent values of η_{elec} for PHB-producing strains are shown in Fig. S13. Fig. 3B shows the values calculated based on $OD_{biomass}$ excluding the light scattering from PHB accumulation. Because of the volatile nature of isopropanol, C_4, and C_5 alcohols, the efficiency of their production may be underestimated due to evaporation. Since C_4 and C_5 alcohols were produced together from the same strain of *R. eutropha*, the combined efficiency for both chemicals was calculated.

The reported efficiencies are not sensitive to the change of temperature and concentrations within our experimental conditions based on the following calculations. The uncertainty of the reported efficiencies at experimental conditions was determined from the following two relationships,

$$\left(\frac{\partial G}{\partial T}\right)_{P,C_i} = -\Delta S$$

$$\Delta(\Delta_r G) = \sum_i RTln(C_i^n)$$

where $\Delta(\Delta_r G)$ is the difference in the Gibbs free energy under our conditions as compared to standard conditions. The entropy changes of gaseous species (CO_2, O_2) are assumed to be the only contributors. The calculated percentages of Gibbs free energy differences are listed below.

Effect of temperature

	Biomass	PHB	Isopropanol (C_3)	Isobutanol (C_4)	Isopentanol (C_5)
$\Delta_r S^o\ (J \cdot mol^{-1} \cdot K^{-1})$	–3.90	70.5	284	378	473
$-\Delta_r S^o \cdot \Delta T\ (J \cdot mol^{-1})$	19.5	–353	-1.42×10^3	-1.89×10^3	-2.36×10^3
$\frac{-\Delta_r S^o \cdot \Delta T}{\Delta_r G^o} \times 100\%$	0.0041%	–0.019%	–0.073%	–0.073%	–0.071%

Effect of concentration

	Biomass	PHB	Isopropanol (C_3)	Isobutanol (C_4)	Isopentanol (C_5)
$\Delta(\Delta_r G)\ (kJ \cdot mol^{-1})$	6.22	–17.9	–29.4	–38.2	–44.6
$\frac{\Delta(\Delta_r G)}{\Delta_r G^o} \times 100\%$	0.13%	–0.94%	–1.5%	–1.5%	–1.3%

Calculation of equivalent gas consumption. The amount of CO_2 assimilated per liter of culture per day is calculated as:

$$N_{CO_2}(\text{mol L}^{-1}\ \text{day}^{-1}) = \frac{(OD_{final} - OD_{before}) \times 0.448\ \text{g L}^{-1}}{24.97\ \text{g mol}^{-1} \times 5\ \text{day}}$$

Here 24.97 g/mol is the effective molecular weight of biomass with the empirical formula $CH_{1.77}O_{0.49}N_{0.24}$ (*39*).

The equivalent volume of air at standard condition is:

$$V\,(L) = \frac{N_{CO_2} \times 22.4\ L/mol}{400\ ppm} \times 1\ L \times 1\ day$$

where the CO_2 concentration in the atmosphere is assumed to be 400 ppm. To assimilate such amount of CO_2, the amount of energy cost should be calculated as:

$$W\left(kWh\ L^{-1}\ day^{-1}\right) = \frac{Charge\ \left(C\ L^{-1}\ day^{-1}\right) \times V_{cell}}{3.6\times10^{6}\ J\ kWh^{-1}}$$

where V_{cell} (L) is the liquid volume of bioelectrochemical reactor.

Model of H_2-dependent growth of *R. eutropha*. The governing equations of H_2-dependent growth are based on the Monod equations (*36*) and the mass balance in an enclosed reactor (*44*). Bacterial growth μ is defined as:

$$\mu \equiv \frac{1}{X_a}\frac{dX_a}{dt} = \mu_{max}\frac{S}{K+S} - b$$

where X_a is the concentration of active biomass, μ_{max} the maximum growth rate, S the concentration of substrate H_2, K the concentration of H_2 at $0.5\mu_{max}$, and b the maintenance term for the microorganism. Mass balance requires:

$$\frac{dS}{dt} = -r_{max}\frac{S}{K+S}X_a + \frac{I}{2FV}$$

where r_{max} is the maximum H_2 consumption rate, I the current of water splitting, F the Faraday's constant, and V the headspace volume of reactor. Based on these two equations, Fig. 2D and S12 were plotted in a dimensionless fashion.

Table S1. Efficiencies and titers for different E_{appl} and experimental conditions. Unless noted specifically, the efficiencies are reported as averaged values over 5~6 days for biomass accumulation with 100% CO_2 in the headspace.

Strain [a]	E_{appl} (V)	Cathode|Anode	V (mL) [b]	C_{buffer} (mM) [c]	η_{elec} [d]	η_{SCE} [d]	Titer (mg/L)
H16	3.0	NiMo|CoP_i	100	36	5.0 ± 0.6 %	0.9 ± 0.1 %	-
H16	2.7	SS|CoP_i	100	36	12 ± 2 %	2.2 ± 0.3 %	-
H16	2.2	NiMo|CoP_i	100	36	no growth	no growth	-
H16	2.2	SS|CoP_i	100	36	no growth	no growth	-
H16	2.0	NiMo|CoP_i	100	36	no growth	no growth	-
H16	2.0	SS|CoP_i	100	36	no growth	no growth	-
H16	2.2	Co-P|CoP_i-CC	100	36	36 ± 8 %	6.4 ± 1.4 %	-
H16	2.2	Co-P|CoP_i-CC	1000	36	30 ± 6 %	5.4 ± 1.1 %	-
BC4 [e]	2.2	Co-P|CoP_i-CC	100	36	38 ± 11 %	6.9 ± 1.9 %	-
H16	2.0	Co-P|CoP_i-CC	100	36	pure CO_2:[f] 54 ± 4 % Air:[f] 20 ± 3 %	9.7 ± 0.8 % 3.6 ± 0.5 %	-
H16	2.0	Co-P|CoP_i-CC	1000	36	47 ± 2 %	8.5 ± 0.3 %	-
BC4 [e]	2.0	Co-P|CoP_i-CC	100	36	42 ± 11 %	7.5 ± 2.0 %	-
H16	1.8	Co-P|CoPi-CC	100	36	no growth	no growth	-
H16	1.8	Co-P|CoP_i-CC	100	108	28 ± 9 %	5.1 ± 1.6 %	-
H16 [g]	2.0	Co-P|CoP_i-CC	100	36	Biomass: 7 ± 2 % [h] PHB: 36 ± 3 % 42 ± 2 % [j]	1.3 ± 0.4 % [h] 6.4 ± 0.5 % 7.6 ± 0.3 % [j]	701 ± 66 [i]
Re2133-pEG12	2.0	Co-P|CoP_i-CC	100	36	Biomass: 13 ± 4 % C_3: 31 ± 4 % [k] 39 ± 2 % [j,k]	2.3 ± 0.8 % 5.6 ± 0.8 % [k] 7.1 ± 0.3 % [j,k]	584 ± 53 [l]
Re2410-pJL26	2.0	Co-P|CoP_i-CC	100	36	biomass: 13 ± 4 % C_4+C_5: 16 ± 2 % [k] 27 ± 4 % [j,k]	2.3 ± 0.6 % 2.9 ± 0.3 % [k] 5.0 ± 0.7 % [j,k]	231 ± 44 [m]

[a] Organism: *R. eutropha*. [b] Liquid volume of bioelectrochemical reactor. [c] Overall concentration of phosphate buffer in the minimal medium solution. Concentration of bicarbonate is not accounted. [d] Unless noted in specific, the values are for biomass accumulation. [e] ROS-tolerant strain. [f] The gaseous composition in the headspace. [g] PHB synthesis under nitrogen-liming condition. [h] After subtracting the light scattering from PHB accumulation (*vide supra*). [i] Titer of PHB bio-plastic. [j] Maximum efficiency within 24-hour periods. [k] Potentially under-estimated owing to the volatile nature of alcohols. [l] Titer of isopropanol (C_3). [m] Combined titer of isobutanol (C_4) and 3-methyl-1-butanol (C_5).

Table S2 Genetic polymorphisms found between the wild-type H16 *R. eutropha* and ROS-tolerant BC4 strain. Two single nucleotide polymorphisms and two deletion events were observed. The large deletion from acrC1 may argue for a decrease in overall membrane permeability, possibly affecting superoxide entry to the cell. The genome sequences are accessible at the NCBI SRA database under the accession number SRP073266.

Mutation	Position	Annotation	Gene	Description
G → T	611,894	R133R	acrC1	cation/multidrug efflux system outer membrane protein
Δ45 bp	611,905	344-388 of 1494 nt	acrC1	cation/multidrug efflux system outer membrane protein
G → A	2,563,281	intergenic, (-1/+210)	Hfq and H16_A2360	uncharacterized host factor I protein/GTP-binding protein
Δ15 bp	241,880	363-377 of 957 nt	H16_B0214	transcriptional regulator, LysR-Family

Table S3. Comparison to other bioelectrochemical systems for CO_2 fixation. As a comparison, the data of this work are listed as well.

Organism/strain	E_{cell} (V)	$N_{reactor}$ [a]	O_2 tolerance [b]	V (mL)	Product	η_{elec} [c]	η_{SCE} [d]	Titer (mg/L)	Source
Methanobacterium palustre [e]	–	2	no	250	CH_4	–	–	~40 [f]	(*12*)
Methanosarcina barkeri	–	2	no	150	CH_4	–	0.07 % [g]	460 [f]	(*14*)
Sporomusa ovata	–	2	no	200	acetate	–	–	~270	(*11*)
S. ovata	3.0 1.9	2 1	no no	200 1000	acetate	30 % 50 %	5.4 % 9 %	~135 ~20	(*45*)
S. ovata	–	2	partial [h]	20	acetate	–	0.38 % [i]	1200	(*13*)
Mostly *Clostridiales* [j]	–	3 [k]	no	200	acetate	–	–	13500	(*46*)
Microbiome [l]	–	2	no	75	acetate	–	–	10500	(*48*)
R. eutropha H16	~5	1	yes	1000	biomass	4.8 %	0.9 %	-	(*49*)
R. eutropha LH74D	~4	1	yes	350	biomass C_4 alcohol C_5 alcohol	1.8 % C_4+C_5: 0.5 % [m]	0.3 % 0.1 % [m]	- ~100 ~50	(*10*)
R. eutropha H16	2.7	1	yes	35	biomass	13 %	2.3 %	-	(*18*)
R. eutropha Re2133-pEG12	3.0	1	yes	35	biomass C_3 alcohol [n]	4.6 % 1.3 %	0.8 % 0.3 %	216	(*18*)
R. eutropha H16	2.0	1	yes	100 1000	biomass	54±4 % 47±2 %	9.7±0.8 % 8.5±0.3 %	-	this work
R. eutropha H16	2.0	1	yes	100	PHB	36±3 %	6.4±0.5 %	701±66	this work
R. eutropha Re2133-pEG12	2.0	1	yes	100	C_3 alcohol [n]	31±4 %	5.6±0.8 %	584±53	this work
R. eutropha Re2410-pJL26	2.0	1	yes	100	C_4+C_5 alcohol	16±2 % [m]	2.9±0.3 % [m]	231±44 [m]	this work

[a] Number of electrochemical compartments in the setup, "1" for one-compartment setup (membrane-less), "2" for two-compartment setup (H-cell). [b] Oxygen tolerance of the CO_2-fixation part of the system. [c] Defined in Methods. Not available in some literature because of the three-electrode setup, which obviated the reaction kinetics of water oxidation reaction. [d] Experimental values if possible. Otherwise the equivalent solar-to-organic efficiencies as defined in Methods are cited. [e] Predominant species in a mixed culture. [f] Calculated as the weight of methane generated per liter of culture, since methane is not soluble in water. [g] Experimentally determined solar-to-organic efficiencies based on InP photocathode and TiO_2 photoanode. [h] The microbes were strictly anaerobes, but the nanowire structure of electrodes provided O_2 tolerance. [i] Experimentally determined solar-to-organic efficiencies based on Si photocathode and TiO_2 photoanode. [j] A pre-enriched mixed microbial community dominated by *Clostridiales* (*47*). [k] A saline extraction compartment is included to extract the produced acetate. [l] Mostly *Acetobacterium* spp. in the granules and *Sulfurospirillum* spp. in the supernatant. [m] Efficiency that combines the yield of both isobutanol (C_4) and 3-methyl-1-butanol (C_5). [n] C_3 alcohol: isopropanol.

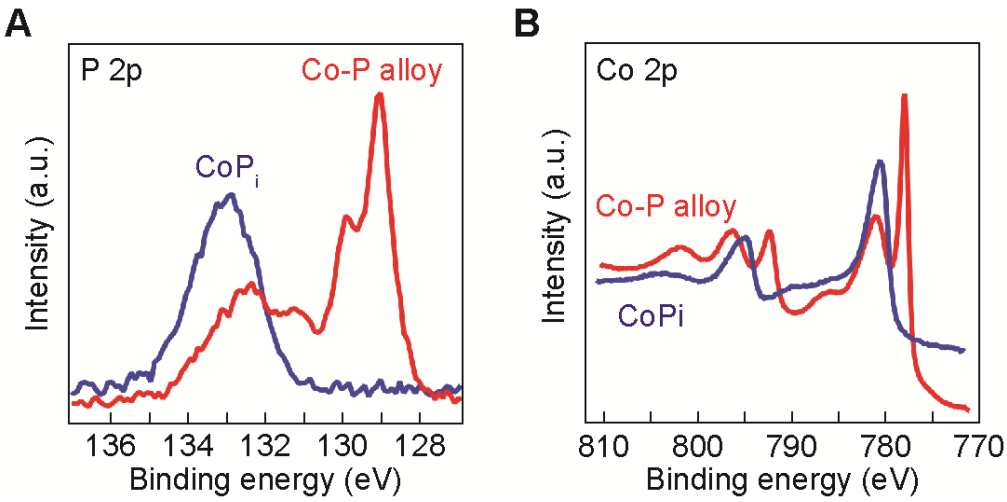

Figure S1. XPS characterizations for Co-P alloy HER cathode for P 2p (**A**) and Co 2p (**B**) signals. As a comparison, the signals of CoP_i OER anode are also presented. The lower binding energy of P 2p in Co-P alloy indicates lower oxidation states of P in the alloy. And similarly the lower binding energy of Co 2p in Co-P demonstrates the presence of metallic Co.

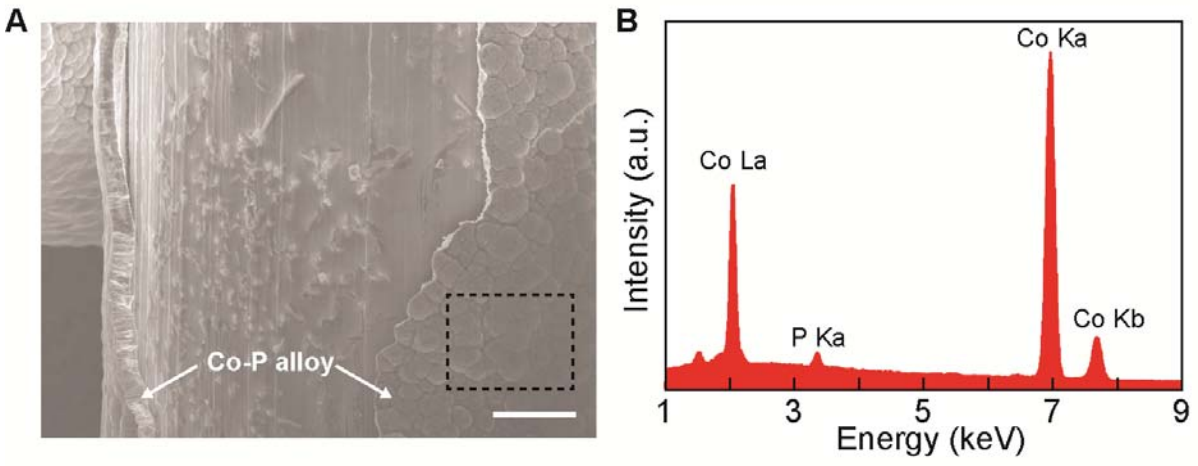

Figure S2. SEM images (**A**) and EDX spectroscopy characterizations (**B**) of Co-P alloy HER catalyst, deposited on stainless steel mesh. Based on the characterization of EDX spectroscopy, there are 6 wt% of phosphorous in the alloy. The measurement of EDX spectroscopy was performed within the dashed rectangle shown in **A**. Scale bar, 20 μm.

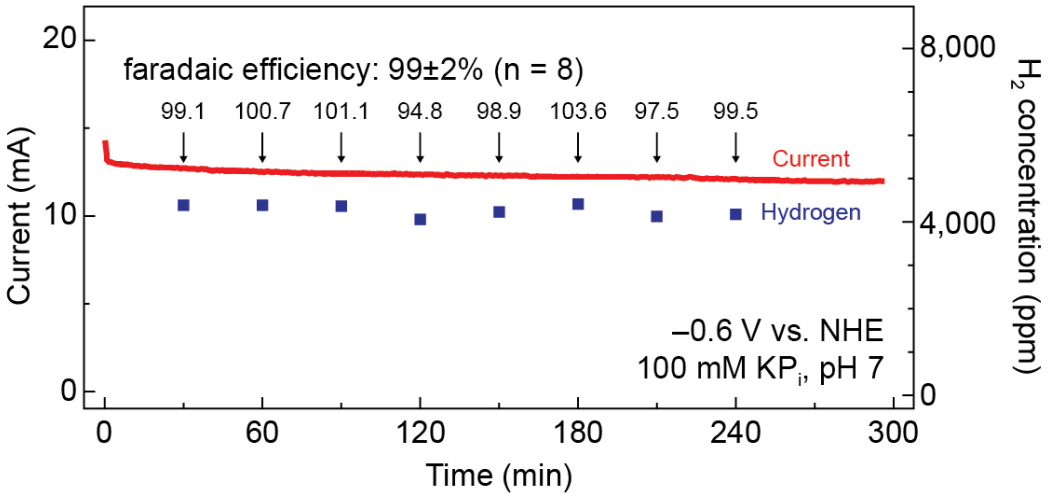

Figure S3. Determination of faradaic efficiency of HER for Co-P alloy cathode in 0.1 M KP_i (pH 7). The electrode was held at constant potentials (–0.6 V *vs.* NHE, normal hydrogen electrode) for HER. Ar gas was bubbled at constant flow rate (20 mL/min) through the cathode chamber of the electrochemical reactor, and the concentration of evolved H_2 in the downstream Ar flow was quantified every 30 min). The H_2 concentrations of individual measurements are also displayed.

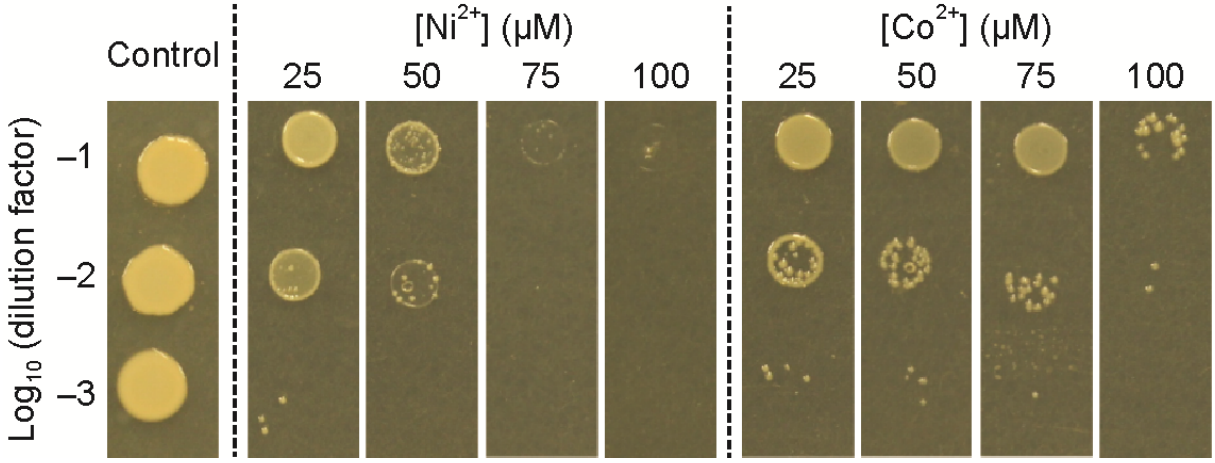

Figure S4. Spot assay of *R. eutropha* for different concentrations of Ni^{2+} and Co^{2+} cations. Cultures treated with different toxicant concentrations for 24 hours were sampled and grown on plates with different dilution factors. At 1/100 dilution, the toxicities of transition metals are visible when the concentration of Ni^{2+} and Co^{2+} are higher than 25 μM ($IC_{50} \sim 25$ μM).

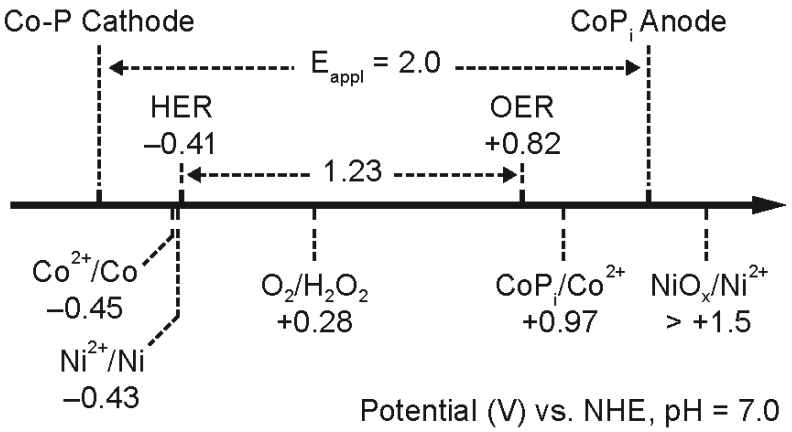

Figure S5. Thermodynamic potentials of various redox couples *vs.* NHE. The potentials of HER cathode and OER anode under E_{appl} = 2.0 V are also listed. The overpotentials are 0.30 V for HER and 0.47 V for OER at E_{appl} = 2.0 V.

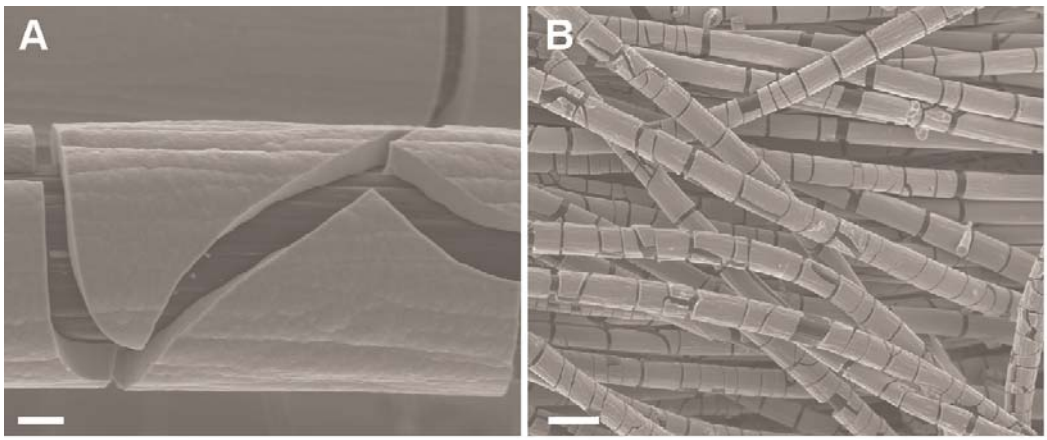

Figure S6. SEM images of CoP_i OER catalyst, deposited on carbon cloth as a high surface-area conductive support. Scale bar, 2 μm (**a**) and 20 μm (**b**).

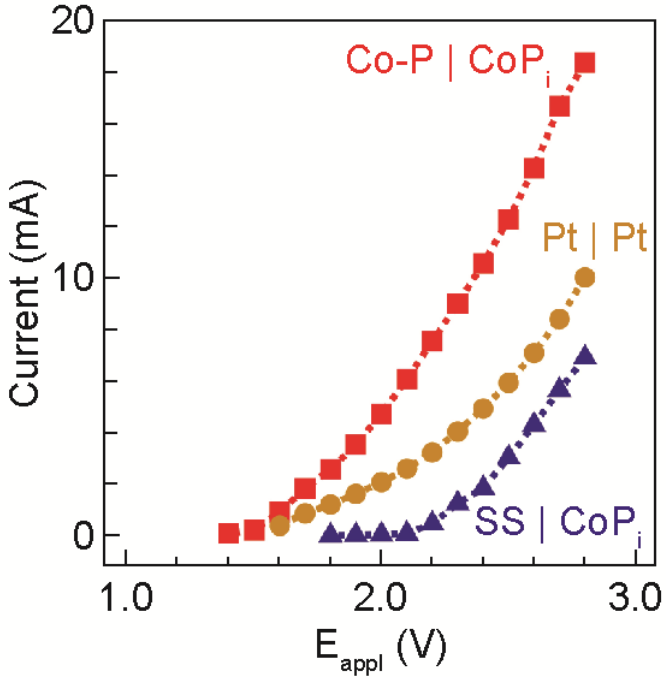

Figure S7. *I-V* characteristics of abiotic water splitting with different catalyst systems. Each data point was collect as the average of 30 min experiment under constant E_{appl}.

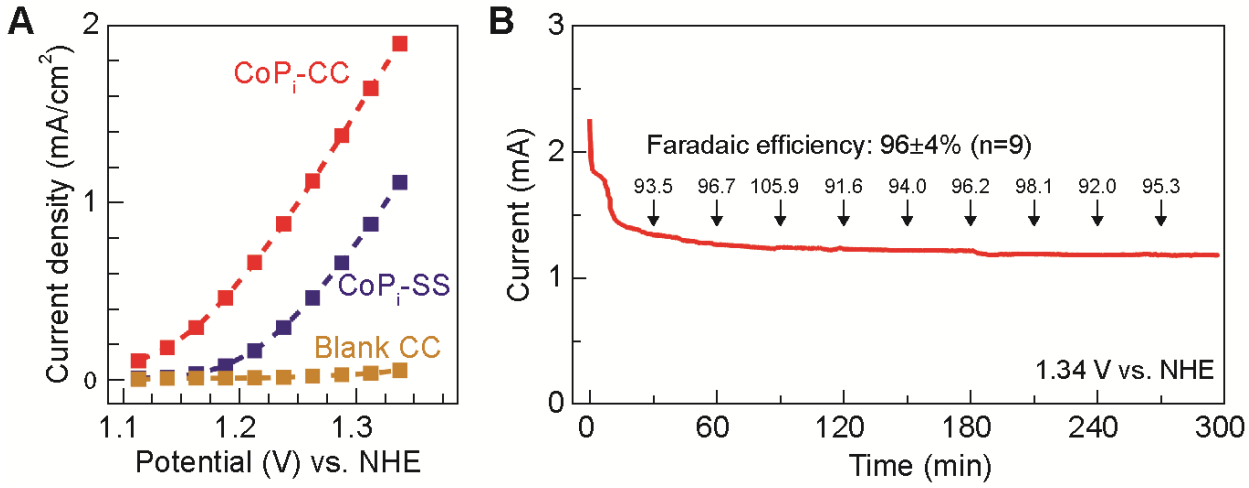

Figure S8. Characterization of CoP_i OER anode loaded on carbon cloth substrate. The high surface area of carbon cloth (CC) yields higher current density than stainless steel mesh (SS). And the water oxidation is stoichiometric without noticeable oxidation of carbon cloth. **A**, Averaged current density based on 30 min chronoamperometry measurement. 0.1 M P_i buffer (pH 7.0). **B**, A long-term chronoamperometry measurement coupled with GC to determine the Faradaic efficiency of water oxidation with 9 replicates (n = 9).

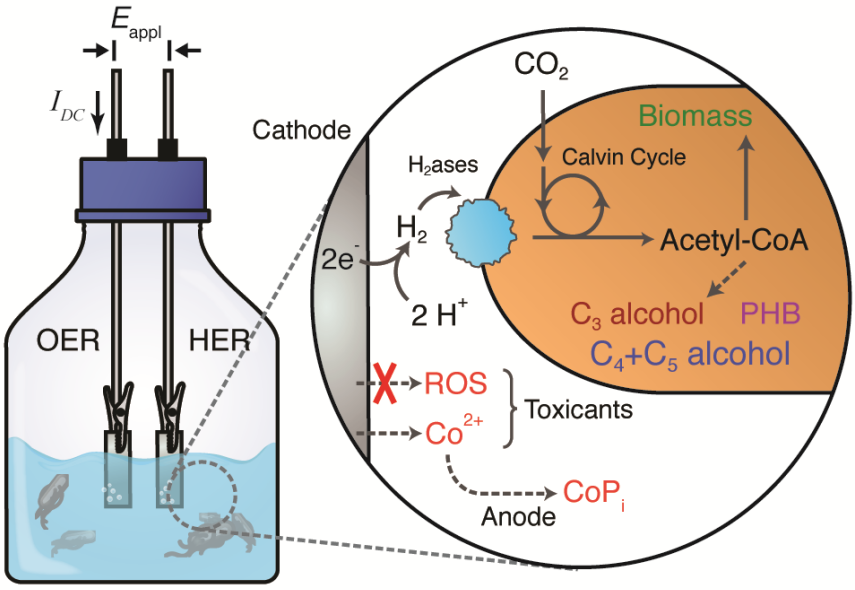

Figure S9. Schematic of hybrid bioelectrochemical system for CO_2 fixation. In this system, electrochemical water splitting produces H_2 as energy intermediate, which is oxidized by hydrogenases (H_2ases) and fuels *R. eutropha* in the same reactor to assimilate CO_2 through Calvin-Benson-Bassham pathway to produce biomass and a variety of organic compounds. The biocompatible water splitting catalyst systems minimizes the generation of ROS and salvages the leach Co^{2+} by the self-healing CoP_i OER catalysts. PHB: poly(3-hydroxybutyrate); C_3: isopropanol; C_4: isobutanol; C_5: 3-methyl-1-butanol.

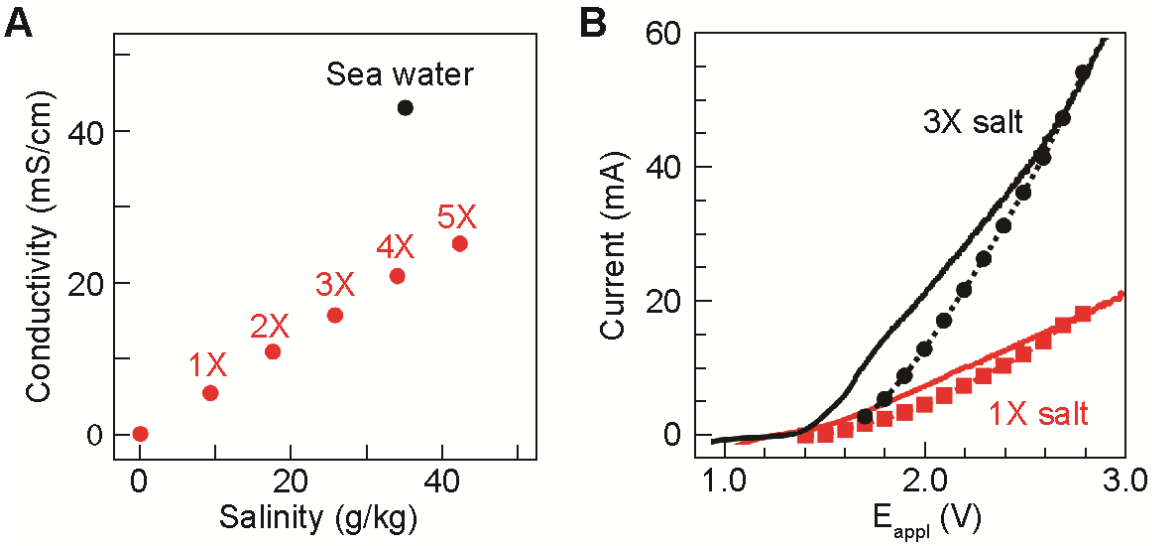

Figure S10. Increased electrochemical water-splitting currents in solutions of higher salinity. **A**, The electric conductivities of solution at different salinities. The default culture solution is denoted as "1X" with 36 mM phosphate buffer. The solution with n-fold phosphate buffer concentration is denoted as "nX". The data of seawater is included as a reference. **B**. Linear scan voltammetry and chronoamperometry data for 1X and 3X solutions. Higher salt content in the solution allows higher current density at the same E_{appl}, by relieving the mass transport constraints. Reported with Co-P cathode and CoP_i-CC anode in a two-electrode abiotic configuration.

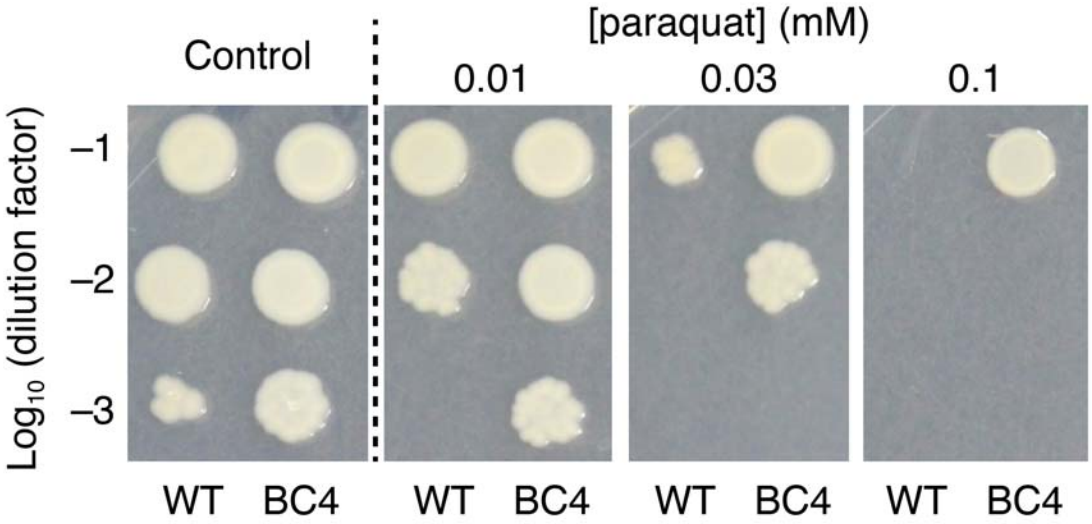

Figure S11. Comparison of ROS tolerance between wild-type H16 (WT) and a ROS-resistant strain (BC4). Paraquat was used an effective ROS inducer. Cultures treated with different paraquat concentrations for 48 hours were sampled and grown on plates with different dilution factors.

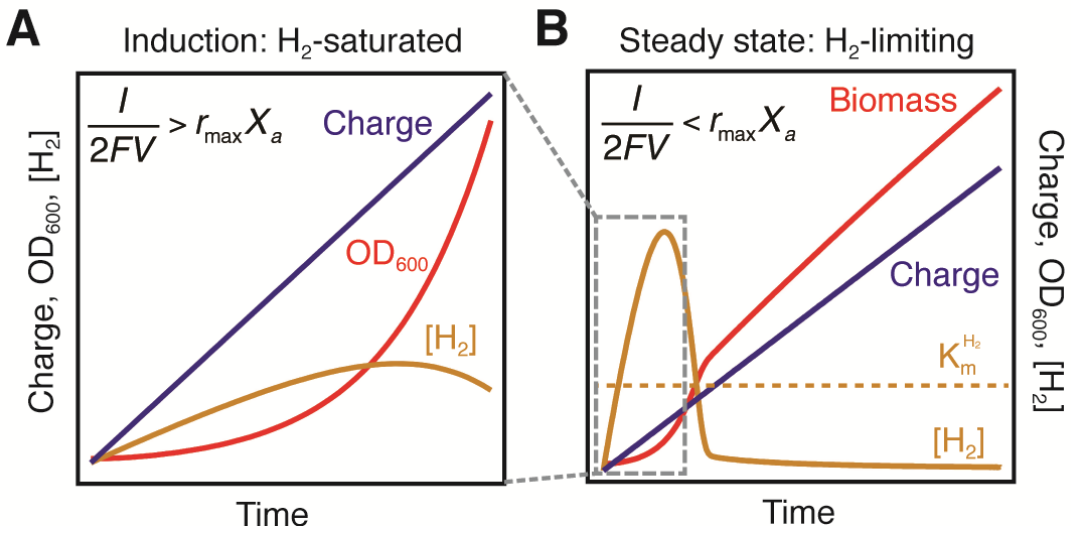

Figure S12. Model for the H_2-dependent growth of *R. eutropha*. The mathematical details of the model are described in the Methods. There is an induction period (**A**), during which the bacteria grows exponentially and the concentration of H_2 is not limiting. As the biomass accumulates, the H_2 concentration will be the limiting factor and fall below the Michaelis constant ($K_m^{H_2}$). Subsequently a linear growth will be observed (**B**). Please note that [H_2] are not drawn at the same scale in **A** and **B**.

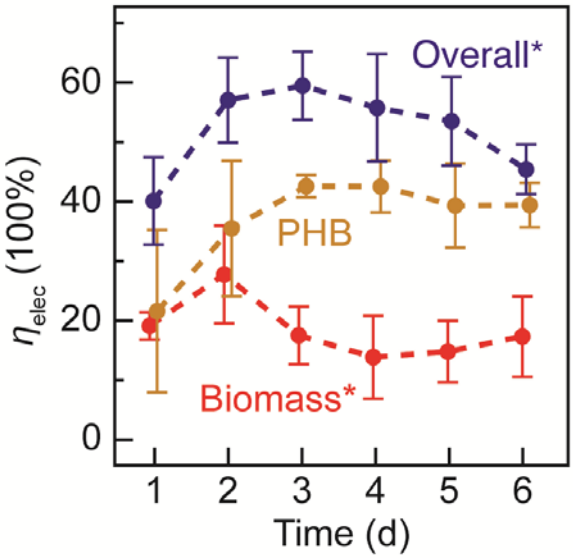

Figure S13. η_{elec} in Fig. 3B before excluding the light scattering from PHB accumulation. The η_{elec} values shown here for biomass formation are calculated based on the measured OD_{600} values that are overestimated by the accumulation of PHB. A correction procedure (*vide supra*) was applied to subtract this interference. The values displayed in Fig. 3B and Table S1 reflect this correction.

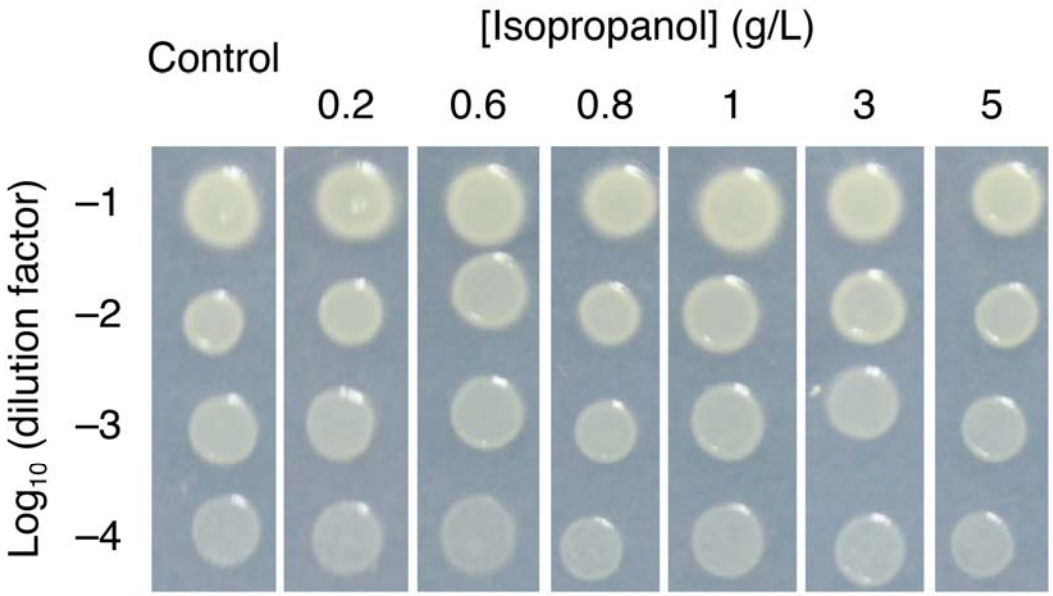

Figure S14. Tolerance of *R. eutropha* at various concentrations of isopropanol. Cultures treated with various isopropanol concentrations for 48 hours were sampled and grown on plates with different dilution factors. For isobutanol (C_4), *R. eutropha* strains similar as the ones used in this work are known to tolerate the alcohol up to 4 g/L (*33*).

Additional references

34. Y. Surendranath, M. Dincă, D. G. Nocera, *J. Am. Chem. Soc.* **131**, 2615 (2009).
35. A. J. Esswein, Y. Surendranath, S. Y. Reece, D. G. Nocera, *Energy & Environmental Science* **4**, 499 (2011).
36. B. E. Rittmann, P. McCarty, L., *Environmental Biotechnology: Principles and Applications*. (McGraw Hill, 2001).
37. K. M. Fagerbakke, M. Heldal, S. Norland, *Aquat. Microb. Ecol.*, **10**, 15 (1996)
38. D. Deatherage, J. Barrick, in *Engineering and Analyzing Multicellular Systems,* L. Sun, W. Shou, Eds. (Springer New York, 2014), vol. 1151, pp. 165-188.
39. R. Grosz, G. Stephanopoulos, *Biotechnol. Bioeng.* **25**, 2149 (1983).
40. J. M. Park, T. Y. Kim, S. Y. Lee, *BMC systems biology* **5**, 101 (2011).
41. S. J. Sim *et al.*, *Nat Biotech* **15**, 63 (1997).
42. S. K. Hahn, Y. K. Chang, S. Y. Lee, *Appl. Environ. Microbiol.* **61**, 34 (1995).
43. A. Ishizaki, K. Tanaka, *J. Ferment. Bioeng.* **71**, 254 (1991).
44. O. Levenspiel, *Chemical Reaction Engineering*. (John Wiley & Sons, ed. 3rd, 1999).
45. C. G. S. Giddings, K. Nevin, T. Woodward, D. R. Lovley, C. S. Butler, *Frontiers in Microbiology* **6**, 468 (2015).
46. S. Gildemyn, *et. al.*, *Environ. Sci. Technol. Lett.* **2**, 325 (2015).
47. S. A. Patil, *et. al.*, *Environ. Sci. Technol.* **49**, 8833 (2015).
48. C. W. Marshall, D. E. Ross, E. B. Fichot, R. S. Norman, H. D. May, *Environ. Sci. Technol.* **47**, 6023 (2013)
49. H. G. Schlegel, R. Lafferty, *Nature* **205**, 308 (1965).